Restoration of Images
Scanned in the Presence of Vibrations

George Wolberg

Department of Computer Science
City College of New York / CUNY
New York, NY 10031
wolberg@cs-mail.engr.ccny.cuny.edu

Robert P. Loce

Xerox Corporation
Corporate Research and Technology
Webster, NY 14580
rloce@wb.xerox.com

Abstract

Images scanned in the presence of mechanical vibration are subject to artifacts such as brightness fluctuation and geometric warping. The goal of the present study is to characterize these distortions and develop a restoration algorithm to invert them, hence producing an output digital image consistent with a scanner operating under ideal uniform motion conditions. The image restoration algorithm described in this paper makes use of the instantaneous velocity of the linear sensor array to reconstruct an underlying piecewise constant or piecewise linear model of the image irradiance profile. That reconstructed image is then suitable for resampling under ideal scanning conditions to produce the restored output digital image. We demonstrate the algorithm on simulated scanned imagery with typical operating parameters.

Keywords: image defects, scanned documents, vibrations, motion quality, image restoration, document restoration

---

Appears in: Journal of Electronic Imaging, vol. 5, no. 1, January 1996.
The first author was supported in part by the NSF (Presidential Young Investigator Award IRI-9157260), PSC-CUNY (RF-666338), and the Xerox Foundation.

1. Introduction

In a document scanner, a linear sensor array (LSA) passes over a document, ideally, at uniform velocity. The output of a single photosensor in the LSA is proportional to the integrated irradiance received by the sensor as it scans through an exposure region. When vibratory motion of the sensor array is considered, the actual size of the exposure region is time-varying. This introduces artifacts such as brightness fluctuation and geometric warping. In this paper, we characterize these artifacts and develop a digital image restoration algorithm to invert these distortions and produce output consistent with a scanner that is not subjected to vibrations.

The effect of motion on the resolution of *analog* imaging systems has been studied extensively. The problem typically addressed concerns characterization of the image blur caused by motion during the integration time of a photosensitive imaging medium. In this typical case the blur is usually constant throughout the image and may be caused by linear or vibratory motion. The blur is constant because the devices under study acquire the full spatial extent of the image at one time, as in a conventional photographic camera. Characterization of this spatial uniform blur leads to a deconvolution-type image restoration algorithm. The present paper differs from that body of work in that we are concerned with images that are digitized in a scanline fashion where each scanline may be acquired with a different arbitrary velocity of the light sensing array. For more information on the uniform blur case see [1, 2, 3].

Several authors have considered the effects of nonuniform photoreceptor motion and other sources of noise in slit scanning photocopiers and digital printers. Loce and Lama [4] characterized the periodic exposure level error caused by vibration in a slit scanning photocopier. Bestenreiner, Geis, Helmberger, and Stadler [5], Takiguchi, Miyagi, Okamura, Ishoshi, and Shibata [6], and Haas [7] examined the effects of periodic scanline position errors when printing periodic binary patterns (e.g., halftones). Schubert [8] and Firth, Kessler, Muka, Noar and Owens [9] analyzed banding in continuous tone prints due to periodic errors. Burns, Rabbani and Ray [10], and Melnychuck and Shaw [11] concentrated on the effect of random errors in the continuous tone and binary cases, respectively. Bloomberg and Engeldrum [12] analyzed the color error on a print that is caused by random pixel placement errors. Loce and Lama [13] employed exposure and xerographic models to examine vibration induced halftone banding in image bar printers. Loce, Lama and Maltz [14] examined the effects of raster position error in a xerographic laser printer and focused on the parametric dependences of halftone banding in the resulting prints. The present paper is concerned with vibratory motion in input scanners. Characterization of image defects has been briefly discussed by the authors in [15] and the restoration method has been previously outlined in [16].

This paper is organized as follows. Section 2 describes the basic operation of a moving photosensor and the problem of vibrations in input scanners. Section 3 presents an analysis of image defects for several special cases. Typical operating parameters are given in Section 4 to provide the proper context in which to address the problem. In Section 5, we outline the restoration algorithm. This includes a discussion of an imaging model and a point spread function (PSF) needed to render the algorithm tractable. Section 6 extends the algorithm by relaxing the constraints on the PSF. Further improvements are presented in Section 7 by considering other imaging models. Section 8 describes the program used to simulate scanning and perform restoration. Examples are provided in Section 9.

2. The Problem of Vibration in Input Scanners

In this section we review the basic problem of input scanning. First, we consider sampling in the time domain. Then we cast the problem into the spatial domain for uniform and nonuniform velocities.

2.1. Sampling in the Time Domain

Consider the output of a single photosensor in an LSA. Let $H(x)$ be the image irradiance distribution, and let $S(x - X(t))$ be the static photosensor sensitivity profile positioned at $X(t)$ at time t (see Fig. 1).

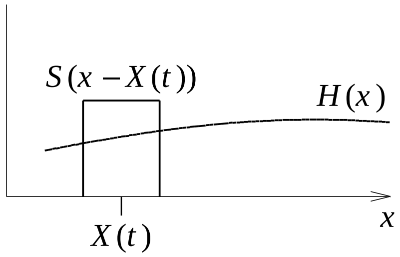

Figure 1: Photosensor sensitivity and image irradiance.

The instantaneous charge $C(X(t))$ generated by the photosensor is given by the product of the irradiance distribution and photosensor sensitivity profile integrated over space:

$$C(X(t)) = \int_{-\infty}^{\infty} H(x)\, S(x - X(t))\, dx \ . \tag{2.1}$$

This cross-correlation integral can be written as a convolution:

$$C(X(t)) = H(X(t)) * S(-X(t)) \ . \tag{2.2}$$

Digitization is performed by integrating, or accumulating, the instantaneous charge for a period of time T_{acc}, and then sampling it at temporal intervals T_s, where $T_{acc} \le T_s$. The value of the nth sample is given by

$$F(n) = \int_{nT_s}^{nT_s + T_{acc}} C(X(t))\, dt = \int_{nT_s}^{nT_s + T_{acc}} H(X(t)) * S(-X(t))\, dt \ . \tag{2.3}$$

The integration in Eq. (2.3) can be replaced by convolution with a $rect$ function to yield

$$\begin{aligned} F(t) &= \sum_n \delta(t - nT_s) \left(rect\left(\frac{t}{T_{acc}} \right) * C(X(t)) \right) \\ &= \sum_n \delta(t - nT_s) \left(H(X(t)) * K(t) \right) \ , \end{aligned} \tag{2.4}$$

where $K(t) = rect(t/T_{acc}) * S(-X(t))$ and

$$rect(t) = \begin{cases} 1 & -0.5 < t \le 0.5 \\ 0 & \text{otherwise} \end{cases} . \tag{2.5}$$

Note that the constant offset in $rect$, i.e., $T_{acc}/2$, has been omitted for notational convenience. Also, note that the array of Dirac delta δ functions allows us to write the collection of samples as a temporal function by sampling the accumulated charge with period T_s.

The accumulated charge is seen to be the convolution of the image irradiance distribution H with a kernel K that combines the effects of sensitivity function S and the motion blur incurred during the accumulation time T_{acc}. While S may be referred to as the *static integration aperture*, we refer to K as the *dynamic integration aperture* because it takes motion blur into account. If we assume that S is rectangular in form and the LSA is moving at uniform velocity during the accumulation time, then K takes a trapezoidal form. Nonuniform velocity gives rise to distortions of the trapezoid.

The sampling electronics digitize an image irradiance distribution over equal intervals in time. It is therefore straightforward to write the collection of samples as a temporal function, as seen above. However, we are interested in the effect of vibratory motion on the digitized image. For the purpose of analyzing image defects, the influence of vibration is best understood by recasting F in terms of spatial coordinate x. The next two sections apply a change of coordinates to the expressions given above to demonstrate the cases of uniform and nonuniform photosensor motion.

2.2. Sampling in the Spatial Domain: Uniform Velocity

Consider the case where the LSA velocity is constant with value V_0. The position function $X(t)$ is

$$X(t) = V_0 t , \tag{2.6}$$

and the instantaneous charge may be written as

$$C(X(t)) = H(X(t)) * S(-X(t)) = H(V_0 t) * S(-V_0 t) . \tag{2.7}$$

Performing the change of variables

$$dX = V_0\, dt , \quad X_s = V_0 T_s , \quad X_{acc} = V_0 T_{acc} , \tag{2.8}$$

the collection of samples in Eq. (2.3) now becomes

$$F(n) = \int_{nT_s}^{nT_s + T_{acc}} H(V_0 t) * S(-V_0 t)\, dt = V_0^{-1} \int_{nX_s}^{nX_s + X_{acc}} H(X(t)) * S(-X(t))\, dX . \tag{2.9}$$

Analogous to the temporal representation, the integration above can be replaced by convolution with a $rect$ function to yield

$$F(X) = V_0^{-1} \left[rect \left[\frac{X}{X_{acc}} \right] * C(X) \right] \sum_n \delta(X - nX_s)$$

$$= V_0^{-1} \left[H(X) * K(X) \right] \sum_n \delta(X - nX_s) , \qquad (2.10)$$

where $K(X) = rect(X / X_{acc}) * S(-X)$. Again, an idealized rectangular approximation of S results in a trapezoidal form for K.

2.3. Sampling in the Spatial Domain: Nonuniform Velocity

LSA velocity nonuniformity tends to be vibratory (periodic). Consequently, it is convenient to express the velocity $V(t)$ as a Fourier series:

$$V(t) = V_0 + \sum_i A_i \sin(2\pi f_i t + \phi_i) , \qquad (2.11)$$

where A_i, f_i, and ϕ_i are the velocity error amplitude, temporal frequency, and phase, respectively, for the ith frequency component. The LSA position $X(t)$ is determined from the instantaneous velocity $V(t)$:

$$X(t) = \int_0^t V(t') dt' = V_0 t + \sum_i \frac{A_i}{2\pi f_i} \left[\cos(\phi_i) - \cos(2\pi f_i t + \phi_i) \right] . \qquad (2.12)$$

Note that the following inequality holds in practice and is useful for further analysis and approximation:

$$V_0 >> \sum_i A_i . \qquad (2.13)$$

The sum of velocity error amplitudes is typically less than 1% of the nominal velocity V_0.

We can express $F_{vib}(n)$, the samples taken in the presence of vibrations, by substituting $X(t)$ into Eq. (2.3). To recast the integral in spatial coordinates, we change the limits of integration and derive an expression for dt/dX:

$$F_{vib}(n) = \int_{nT_s}^{nT_s+T_{acc}} C(X(t)) dt = \int_{V_0 nT_s + \xi_{n,0}}^{V_0(nT_s+T_{acc})+\xi_{n,1}} C(X(t)) \frac{dt}{dX} dX , \qquad (2.14)$$

where $\xi_{n,0}$ and $\xi_{n,1}$ are the spatial deviations of the LSA from the nominal positions at times nT_s and $nT_s + T_{acc}$, respectively. The limits of integration mark both ends of the span over which the photosensor integration process takes place. The position errors $\xi_{n,0}$ and $\xi_{n,1}$ are defined as

$$\xi_{n,0} = \sum_i \frac{A_i}{2\pi f_i} \left[\cos(\phi_i) - \cos(2\pi f_i n T_s + \phi_i) \right] ,$$

$$\xi_{n,1} = \sum_i \frac{A_i}{2\pi f_i} \left[\cos(\phi_i) - \cos(2\pi f_i n T_s + T_{acc} + \phi_i) \right] . \tag{2.15}$$

The term dt/dX serves to weigh the instantaneous charge with the time exposure for all positions across the accumulation interval. We derive an approximation for dt/dX by taking a first-order truncated Taylor series approximation to the reciprocal of the velocity,

$$\frac{dt}{dX} = V(t)^{-1} \approx V_0^{-1} - V_0^{-2} \sum_i A_i \sin(2\pi f_i t + \phi_i) , \tag{2.16}$$

and substituting the first-order dependence for t, i.e., $t = X/V_0$, in Eq. (2.16). This yields a result that is expressed independently of t:

$$\frac{dt}{dX} = V(t)^{-1} \approx V_0^{-1} - V_0^{-2} \sum_i A_i \sin(2\pi f_i X / V_0 + \phi_i) . \tag{2.17}$$

We thus have

$$F_{vib}(n) = \int_{nX_s + \xi_{n,0}}^{nX_s + X_{acc} + \xi_{n,1}} C(X) \left[V_0^{-1} - V_0^{-2} \sum_i A_i \sin(2\pi\beta_i X + \phi_i) \right] dX , \tag{2.18}$$

where $X_s = V_0 T_s$ is the nominal spatial sampling period and $\beta_i = f_i / V_0$ is the ith spatial frequency of the vibration.

From Eq. (2.18) we see that the nonuniform velocity affects the charge accumulation integral in two ways: the integration limits are changed and a second term appears that is a low amplitude sum of sinusoids. These two respective effects may be thought of as FM and AM modulation of the image signal by the vibration. They are tightly coupled because the sum of sinusoids serves to compensate for the changing integration limits, which vary only because we are integrating in space rather than time. The role of these effects can best be appreciated by considering their influence in maintaining a flat-field response when imaging a region of constant intensity in the presence of vibrations.

We are interested in considering vibration frequencies corresponding to spatial frequencies at which the eye is most sensitive. Because the spatial periods of interest ($1/\beta_i \approx 1$ mm) tend to be long compared to the sampling integration distance ($X_{acc} \approx 0.057$ mm), each sine function may be approximated by its value at the center of the range of integration. This amounts to using a piecewise constant model for the sinusoids. Let

$$\xi_{n,ctr} = \frac{X_{acc} + \xi_{n,1} - \xi_{n,0}}{2} . \tag{2.19}$$

The set of samples becomes

$$F_{vib}(n) = \left(V_0^{-1} - V_0^{-2} \sum_i A_i \sin(2\pi\beta_i (nX_s + \xi_{n,ctr}) + \phi_i) \right) \int_{nX_s + \xi_{n,0}}^{nX_s + X_{acc} + \xi_{n,1}} C(X)\, dX \ . \quad (2.20)$$

Representing this result in spatial form yields an expression similar to Eq. (2.10):

$$F_{vib}(X) = \sum_n W_n \left(rect\left(\frac{X}{2\xi_{n,ctr}} \right) * C(X) \right) \delta(X - nX_s)$$

$$= \sum_n W_n \left(H(X) * K_{vib}(X) \right) \delta(X - nX_s) \ , \quad (2.21)$$

where

$$K_{vib}(X) = S(X) * rect\left(\frac{X}{2\xi_{n,ctr}} \right) \ , \quad (2.22)$$

$$W_n = V_0^{-1} - V_0^{-2} \sum_i A_i \sin(2\pi\beta_i (nX_s + \xi_{n,ctr}) + \phi_i) \ . \quad (2.23)$$

As in the uniform velocity case, an idealized rectangular approximation of S results in a trapezoidal form for K. However, in the present nonuniform velocity case, the dimensions and offset of the trapezoid varies for each sample point. Note that W_n scales the trapezoid such that its height is inversely proportional to its width. A good approximation to W_n is the inverted linear expression $T_{acc} / (X_{acc} + \xi_{n,1} - \xi_{n,0})$.

3. Analysis of Image Defects for Special Cases

In this section, we examine the image artifacts induced by vibrations for several specific image types. The artifacts are examined by deriving the image irradiance viewed by the sensor as a function of time.

3.1. Uniform Input Image

Consider the area sample expression of Eq. (2.3). Because H is constant for a uniform image, the integrand becomes a constant C, and the integral of Eq. (2.3) becomes the constant CT_{acc}. Vibrations do not affect samples taken of a uniform image.

3.2. Linear Input Image

Consider an image with a simple linear ramp spatial irradiance distribution:

$$H(x) = hx, \quad x > 0 \ . \quad (3.1)$$

Assume the LSA position function is given by a sum of sinusoids:

$$X(t) = V_0 t + \sum_i A_i \sin(2\pi f_i t + \phi_i) \ . \quad (3.2)$$

The irradiance observed by the LSA over time may be obtained by substituting the position function into the irradiance distribution,

$$H(X(t)) \;=\; h\; V_0 t \,+ h \sum_i A_i \,\sin(2\pi f_i\, t \,+ \phi_i)\,. \tag{3.3}$$

We see that the vibration introduces frequency components into the irradiance distribution that are equivalent to the vibration frequencies. The amplitudes are scaled by the slope of the input irradiance distribution.

3.3. Sinusoidal Input Image

Consider a sinusoidal input image with spatial frequency ν and phase zero. The irradiance may be written

$$H(x) \;=\; H_0 + h\, \sin(2\pi\nu x)\,. \tag{3.4}$$

To simplify the analysis, assume a single temporal frequency of vibration f with zero phase,

$$X(t) \;=\; V_0 t \,+ A\, \sin(2\pi f t)\,. \tag{3.5}$$

The irradiance observed by the LSA over time may be written by substituting the position expression into the formula for the irradiance distribution,

$$H(X(t)) \;=\; H_0 + h \sin[2\pi\nu(V_0 t \,+ A \sin(2\pi f t))]\,. \tag{3.6}$$

To decompose the irradiance into frequency components, first employ

$$\sin(x + y) \;=\; \sin(x)\cos(y) + \cos(x)\sin(y)\,. \tag{3.7}$$

The irradiance becomes

$$\begin{aligned} H(X(t)) \;=\; & H_0 + h \sin[2\pi\nu V_0 t] \cos[2\pi\nu A\, \sin(2\pi f t))] \\ & + h \cos[2\pi\nu V_0 t] \sin[2\pi\nu A \sin(2\pi f t))]\,. \end{aligned} \tag{3.8}$$

Next, employ the Bessel expansion for sinusoids with sinusoidal arguments [17]:

$$\cos(z \sin(\theta)) \;=\; J_0(z) + 2 \sum_{k=1}^{\infty} J_{2k}(z)\cos(2k\,\theta)\,, \tag{3.9a}$$

$$\sin(z \sin(\theta)) \;=\; 2 \sum_{k=1}^{\infty} J_{2k+1}(z)\sin((2k+1)\theta)\,. \tag{3.9b}$$

The irradiance may be written

$$\begin{aligned} H(X(t)) \;=\; & H_0 \\ & + h \sin[2\pi\nu V_0 t] \left(J_0(2\pi\nu A) + 2 \sum_{k=1}^{\infty} J_{2k}(2\pi\nu A)\cos[(2k)(2\pi f t)] \right) \\ & + h \cos[2\pi\nu V_0 t] \left(2 \sum_{k=0}^{\infty} J_{2k+1}(2\pi\nu A)\sin[(2k+1)(2\pi f t)] \right) \end{aligned}$$

$$= H_0 + h\sin[2\pi\nu V_0 t]\, J_0(2\pi\nu A)$$
$$+ 2h\sum_{k=1}^{\infty} J_{2k}(2\pi\nu A)\cos[(2k)(2\pi f t)]\sin[2\pi\nu V_0 t]$$
$$+ 2h\sum_{k=0}^{\infty} J_{2k+1}(2\pi\nu A)\sin[(2k+1)(2\pi f t)]\cos[2\pi\nu V_0 t]\,. \qquad (3.10)$$

To arrive at an expression with additive sinusoidal components, employ

$$\cos(x)\sin(y) \;=\; \frac{\sin(x+y) - \sin(x-y)}{2}\,. \qquad (3.11)$$

The irradiance may be written as

$$H(X(t)) \;=\; H_0 + h\sin[2\pi\nu V_0 t]\, J_0(2\pi\nu A)$$
$$+ h\sum_{k=1}^{\infty} J_{2k}(2\pi\nu A)\left(\sin[(2k)(2\pi f t) + (2\pi\nu V_0 t)] - \sin[(2k)(2\pi f t) - (2\pi\nu V_0 t)]\right)$$
$$+ h\sum_{k=0}^{\infty} J_{2k+1}(2\pi\nu A)\left(\sin[(2k+1)(2\pi f t) + (2\pi\nu V_0 t)] + \sin[(2k+1)(2\pi f t) - (2\pi\nu V_0 t)]\right)$$

$$= H_0 + h\sin[2\pi\nu V_0 t]\, J_0(2\pi\nu A)$$
$$+ h\sum_{k=1}^{\infty} J_{2k}(2\pi\nu A)\left(\sin[(2\pi t)(2kf + \nu V_0)] - \sin[(2\pi t)(2kf - \nu V_0)]\right)$$
$$+ h\sum_{k=0}^{\infty} J_{2k+1}(2\pi\nu A)\left(\sin[(2\pi t)(2k+1)f + \nu V_0)] + \sin[(2\pi t)((2k+1)f - \nu V_0)]\right)\,. \qquad (3.12)$$

We see that the irradiance distribution is given by the input sinusoidal distribution, scaled by a constant, plus a scaled component at the vibration frequency, plus a series of ‘‘beats’’ between the vibration frequency and input image frequency. To more clearly see the beat effect, we examine the lowest order terms. Using only the lowest order terms of each series, H becomes

$$H(X(t)) \;=\; H_0 + h\sin[2\pi\nu V_0 t]\, J_0(2\pi\nu A)$$
$$+ hJ_1(2\pi\nu A)\left(\sin[(2\pi t)(f + \nu V_0)] - \sin[(2\pi t)(f - \nu V_0)]\right)$$
$$+ hJ_2(2\pi\nu A)\left(\sin[(2\pi t)(2f + \nu V_0)] - \sin[(2\pi t)(2f - \nu V_0)]\right)\,. \qquad (3.13)$$

The lowest order beats occur at the sum and difference of the image frequency and vibration frequency, while the second order beats occur at the sum and difference of the image frequency with two times the vibration frequency. Note that the vibration frequency itself is not present in the scanned image. An example showing the effect of vibration on a periodic image is given in Section 9.

4. Typical Parameters

To better motivate the problem and validate its solution, we provide an example of operating parameters for a typical document scanner. This data is also furnished to support the modeling assumptions made in our image restoration algorithm. Consider the following parameters for a 400 dpi scanner:

- An LSA passes over the document at about 2.5 in/second, or 63.5 μm/msec.
- Each photosensor on the array is 7μm × 7μm and has a static field of view of 63.5 μm, for a magnification factor of 0.11023. Note that 63.5 μm could be considered the static dot size.
- The time for acquiring a scanline is 1 msec. Approximately 90% of the time is used for accumulating charge, while the remaining 10% is used for other operations like reading and clearing the charge. Therefore, the accumulation time is 0.9 msec, with accumulations beginning every 1 msec.
- Instantaneous charge generation is linear with the irradiance received by the sensor.
- The actual velocity $V(t)$ of the LSA typically varies less than 1% from the nominal velocity. Because velocity error tends to be vibratory, the variation can be modeled as a sum of sinusoids. Key frequencies to analyze are those that correspond to roughly 1 cycle/mm in the document space. This is due to the high sensitivity of the eye at this frequency. In the case of the typical scanner considered here, the sensitive temporal frequencies are about (1 cycle/mm)×(63.5 mm/sec)×(0.11023), or 7.0 Hz.

The characteristic parameters listed above are used in Fig. 2 to depict the *uniform* motion of an individual photosensor as it passes over a document. The top part of Fig. 2 represents the photosensor fields of view at both ends of each accumulation interval. Solid lines and dashed lines are used respectively to mark these instances. The time at which each interval starts is marked (in msecs) above the appropriate photosensor sites. Because the accumulation time is 0.9 msec and the period between intervals is 1 msec, the fields of view at the ends of each interval overlap. This is a desirable property, permitting us to avoid aliasing artifacts that may occur if the photosensor were not exposed to the intervening area. We assume that all points under the field of view of the sensor are weighted equally. That is, sensitivity function $S(x)$ is a *rect* function with a width of 63.5 μm in the document space.

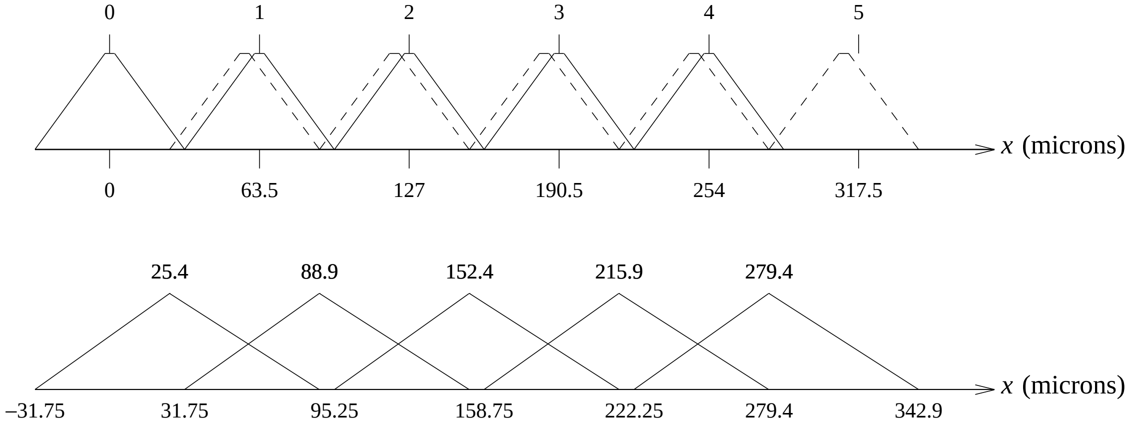

Figure 2: Sampling under uniform photosensor motion. Fields of view at ends of each

accumulation interval (top); integration kernels (bottom).

The accumulation of charge on a single photosensor produces an area sample associated with the region of the document traversed during one accumulation interval. That sample is actually a weighted integral of the underlying irradiance distribution, weighted by kernel K (see Eq. 2.4). The weights reflect the contribution of each point on the irradiance distribution to the accumulated charge. The contribution of a point of the irradiance distribution is computed as the amount of time it is exposed to the moving field of view of the sensor. Due to less exposure time for points at both ends of a sensor's field of view, the kernel shape for the area sample is a trapezoid, and actually, nearly triangular. These kernels are depicted in the bottom of Fig. 2, with labels to mark the positions (in microns) at which the trapezoidal kernels change values. Assuming constant velocity, the top of each trapezoid is flat. Were the static field of view infinitesimally narrow, the kernel would be a scaled *rect* function. As it stands, the kernels refer to K in Eq. (2.4).

Referring back to Fig. 2, we note that at time 0, the photosensor is positioned at 0 μm and ''sees'' the scanline interval between −31.75 μm and 31.75 μm for a field of view of 63.5 μm. As the photosensor moves across the document at 63.5 μm/msec, it integrates the charge produced from the observed image. At the end of the 0.9 msec accumulation time, the photosensor arrives at location 57.15 μm and has a field of view that extends between 25.40 μm and 88.90 μm. The accumulated charge for this first sample is equal to the integral of the underlying irradiance distribution multiplied with kernel K. Accumulation begins again at 1 msec, where the field of view extends from 31.75 μm to 95.25 μm, and continues through 1.9 msec when the charge is sampled. Figure 2 shows the first four accumulation intervals.

5. Image Restoration: Rectangular Kernel K

This section outlines our algorithm for restoring images scanned in the presence of vibrations. We begin by noting several simplifying assumptions and describing an image model that permits our problem to be constrained in a manner that leads to a constructive algorithm. The key assumption made here is that the static integration aperture S is sufficiently narrow so that we may approximate the dynamic integration aperture K to be a *rect* function. This is reasonable for some physical systems and it provides an image restoration algorithm with low computational cost. The area sample problem is treated more fully in Section 6 where we examine the use of a trapezoidal kernel K.

Consider a stream of area samples produced by a photosensor that moves across a document at uniform velocity. Assume that S is sufficiently narrow so that we may approximate the trapezoid kernel K to be a *rect* function. In that case, each area sample is the unweighted integral of the image irradiance function spanned during the charge accumulation time. Furthermore, assume that the accumulation time and the sampling period is the same, i.e., the time needed to read and clear the charge is negligible ($T_{acc} \approx T_s$). Figure 3a shows a set of area samples F_n and the underlying irradiance function H from which they are produced. In this ideal case of uniform LSA velocity, samples produced at regular intervals T_s in time relate to the areas under H at regular intervals in space. When the sensor travels at nonuniform velocity, samples produced at regular intervals in time relate to the areas under H at irregular intervals in space (Fig. 3b). Notice how the same input now yields different output values.

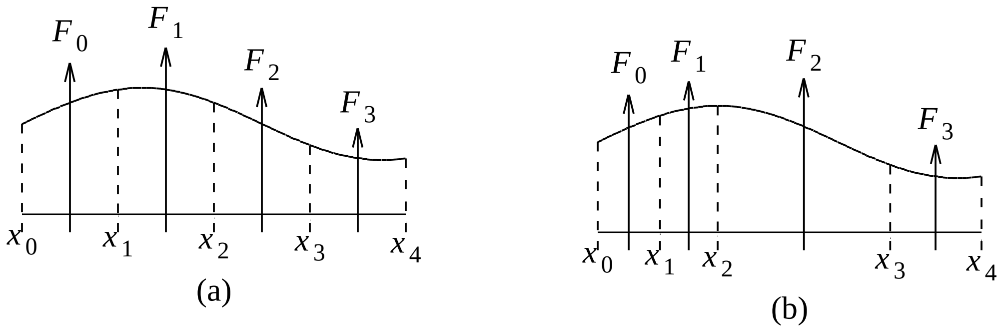

Figure 3: Area samples taken under (a) uniform and (b) nonuniform photosensor velocity.

The image restoration algorithm that we propose infers the underlying image irradiance distribution from the area samples so that we may resample H (or actually re-integrate) at regular intervals in space. Unfortunately, even with precise knowledge of the instantaneous LSA velocity $V(t)$, this problem is underconstrained. Given the nonuniform samples and general image class, it is not possible to infer continuous irradiance data from the sparse area samples because there are an infinite number of irradiance distributions that share the same integral under the respective intervals. For the purpose of algorithm development, we model the irradiance distribution as a linear spline. By modeling H to consist of piecewise linear segments that may change only at regular intervals, it becomes possible to precisely infer H given the area samples F_n and positions x_n that delimit the nonuniform intervals. In practice, this piecewise linear constraint on H is not unreasonable given that the size of the interval is small, e.g., 63.5 μm, and the class of images of interest are continuous tone. When considering the blurring nature of some marking processes and print papers, it may also be reasonable to model halftones and text as a piecewise linear function.

The main task in restoring the image is to recover the control points y_n of the linear spline. Once the control points are determined, H may be reconstructed as a linear spline and area samples can be easily computed at regular intervals. In this manner, we produce output consistent with that of an ideal scanner.

Figure 4 depicts an image irradiance distribution and its linear spline approximation. The control points, shown highlighted, lie at regular intervals $X_s = V_0 T_s$, where V_0 is the nominal velocity and T_s is the sampling period.

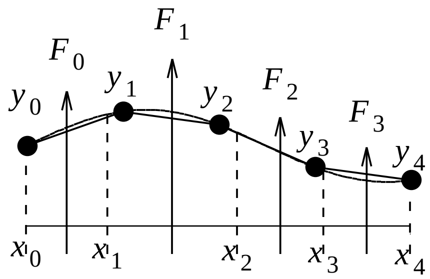

Figure 4: Piecewise linear model.

Before delving into the computation of y_n, we first discuss the relation between area samples and the control points. Area samples and position information are collected at regular time intervals. Due to the chosen image model and the relatively small photosensor position errors, one important assumption that is made here is that two consecutive LSA positions must either lie in the same linear spline segment or straddle two segments. Figure 5 depicts both cases, with points A and B denoting the endpoints of the accumulation interval. The next two sections consider each case and demonstrate how the area samples relate to the unknown linear spline control points we seek to recover.

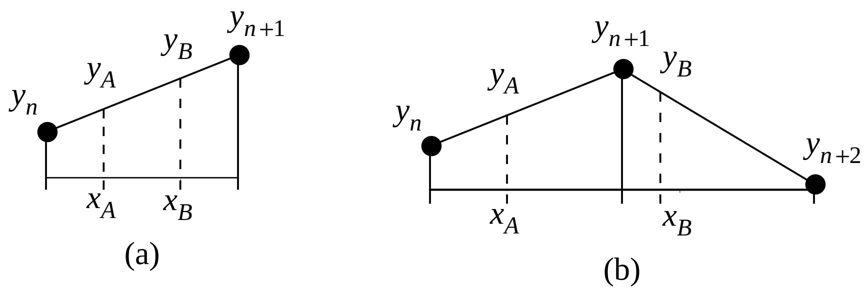

Figure 5: Two area sampling cases.

5.1. Area Samples — Case 1: A and B Lie in One Spline Segment

Consider line segment AB in Fig. 5a. The area sample F_n for that interval is the normalized integral under the line $H(x) = m_H x + b_H$ from x_A to x_B:

$$F_n = W_n \int_{x_A}^{x_B} H(x)\,dx = W_n \left[\frac{m_H}{2} \Delta x^2 + b_H \Delta x \right] = W_n \left[\frac{\Delta y\ \Delta x}{2} + y_A\ \Delta x \right] , \qquad (5.1)$$

where $m_H = \Delta y / \Delta x$, $\Delta y = y_B - y_A$, and $\Delta x = X_{acc} = x_B - x_A$. The normalization term W_n is given in Eq. (2.23). Simplifying F_n further we have

$$F_n = W_n \left[\frac{(y_A + y_B)\,(x_B - x_A)}{2} \right] . \qquad (5.2)$$

It is important to note that we are not actually given y_A or y_B. Instead, they are determined by interpolating between the unknown control points using the known LSA positions x_A and x_B. Without loss of generality, we normalize the parameters so that $x_n = 0$, $x_{n+1} = 1$, and $0 \le x_A, x_B \le 1$, to yield the expressions

$$y_A = y_n (1 - x_A) + y_{n+1} (x_A) , \tag{5.3}$$

$$y_B = y_n (1 - x_B) + y_{n+1} (x_B) . \tag{5.4}$$

Substituting these expressions into Eq. (5.2) yields the following relationship between F_n and the unknown control points:

$$\frac{2 F_n}{W_n} = \left[y_n (2 - x_A - x_B) + y_{n+1} (x_A + x_B) \right] (x_B - x_A)$$

$$= y_n (x_A^2 - x_B^2 - 2x_A + 2x_B) + y_{n+1} (-x_A^2 + x_B^2) . \tag{5.5}$$

We simplify further by factoring out the terms $k_1 = x_A - x_B$ and $k_2 = x_A + x_B$:

$$\frac{2 F_n}{W_n} = y_n \left[k_1 (k_2 - 2) \right] + y_{n+1} \left[-k_1 k_2 \right] . \tag{5.6}$$

Therefore, every measurement of F_n adds another set of constraints on the control points, which we shall solve for using a linear system solver.

5.2. Area Samples — Case 2: *A* and *B* Straddle Two Spline Segments

Again without loss of generality, we normalize the parameters in Fig. 5b so that $x_n = 0$, $x_{n+1} = 1$, $x_{n+2} = 2$, and $0 \le x_A , x_B \le 1$, thus yielding

$$y_A = y_n (1 - x_A) + y_{n+1} (x_A) , \tag{5.7}$$

$$y_B = y_{n+1} (1 - x_B) + y_{n+2} (x_B) . \tag{5.8}$$

F_n is now expressed as the sum of two area contributions:

$$F_n = F_{n1} + F_{n2}$$

$$= W_n \left[\frac{(y_A + y_{n+1}) (1 - x_A)}{2} \right] + W_n \left[\frac{(y_{n+1} + y_B) x_B}{2} \right] , \tag{5.9}$$

where F_{n1} and F_{n2} refer to the area components straddled across the two spline segments. Substituting the expressions for y_A and y_B into Eq. (5.9), we are left with the following expression in terms of the unknown control points:

$$\frac{2F_n}{W_n} = \left[y_n (1-x_A) + y_{n+1} x_A + y_{n+1} \right] (1-x_A) + \left[y_{n+1} + y_{n+1}(1-x_B) + y_{n+2} x_B \right] x_B$$

$$= y_n \left[(1-x_A)^2 \right] + y_{n+1} \left[1 - x_A^2 + (2-x_B) x_B \right] + y_{n+2} \left[x_B^2 \right] . \tag{5.10}$$

5.3. Solving for the Control Points

Given either of the two cases for the positions of A and B, we have Eqs. (5.6) and (5.10) to relate each area sample with the neighboring control points. Collectively, they yield a tridiagonal system of equations $\mathbf{K}\,\mathbf{Y} = \mathbf{F}$:

$$\begin{bmatrix} b_0 & c_0 & & & & \\ a_1 & b_1 & c_1 & & & \\ & a_2 & b_2 & c_2 & & \\ & & \cdot & \cdot & & \\ & & & \cdot & \cdot & \\ & & & a_{n-2} & b_{n-2} & c_{n-2} \\ & & & & a_{n-1} & b_{n-1} \end{bmatrix} \begin{bmatrix} y_0 \\ y_1 \\ y_2 \\ \cdot \\ \cdot \\ y_{n-2} \\ y_{n-1} \end{bmatrix} = \begin{bmatrix} 2F_0/W_0 \\ 2F_1/W_1 \\ 2F_2/W_2 \\ \cdot \\ \cdot \\ 2F_{n-2}/W_{n-2} \\ 2F_{n-1}/W_{n-1} \end{bmatrix} . \tag{5.11}$$

The elements a_i, b_i, and c_i are the weights of y_{i-1}, y_i, and y_{i+1}, respectively, as given in Eqs. (5.6) and (5.10). They are expressed in terms of the known x_A and x_B positions. The first and last rows are influenced by our choice of boundary conditions. For simplicity, we chose to use border replication to determine pixel values that fall outside the domain of the image. That is, $y_{-1} = y_0$ and $y_n = y_{n-1}$. Therefore, if an additional term (c_{n-1}) is needed in the last row of tridiagonal matrix $\mathbf{K}$, that term is added to b_{n-1} because it reflects the influence of the last replicated pixel.

The control points in $\mathbf{Y}$ are evaluated by multiplying the known area samples $\mathbf{F}$ with the inverse of the tridiagonal matrix $\mathbf{K}$. That is, $\mathbf{Y} = \mathbf{K}^{-1}\mathbf{F}$. The inversion of tridiagonal matrix $\mathbf{K}$ has an efficient algorithm that is solvable in linear time [18]. It is important to note that the two cases for the positions of A and B described earlier may be extended. For instance, it is conceivable that A and B span more than two spline segments. The implication of this relaxed condition is that matrix $\mathbf{K}$ would no longer be tridiagonal, i.e., more off-diagonal elements will become nonzero. Efficient methods for solving a band diagonal linear system of equations is demonstrated in the next section, where it is used to handle a trapezoidal shape for kernel K.

6. Image Restoration: Trapezoidal Kernel K

The tridiagonal system of equations derived above is a consequence of two assumptions: consecutive LSA positions never span more than two spline segments, and the LSA sensitivity function S is an impulse (i.e., kernel K is a *rect* function). For the given image model the former assumption is justifiable because the nonuniform LSA velocity generally does not exceed 1% of the nominal velocity. The latter assumption, however, is generally not true since infinitesimaly narrow point spread functions (static integration apertures) are difficult to realize. As shown in Fig. 2, S has a field of view on the order of one dot size, e.g., 63.5 μm for a 400 dpi scanner. Since S has approximately the same width as X_{acc}, kernel K is trapezoidal, and very nearly triangular.

Figure 6a depicts the three intervals of a trapezoid, delimited by points x_0, x_1, x_2, and x_3. Note that the trapezoid extends beyond LSA positions x_A and x_B, thereby widening the accumulation interval. The points delimiting the three trapezoid intervals may be expressed in terms of the field of view (FOV) of each photosensor. In Fig. 2, for instance, $FOV = 1$ dot size. Note that $FOV = 0$ corresponds to the ideal case where S is an impulse and K is a *rect* function. Rectangular S may be described by $S = rect(x / FOV)$. If we let $w = FOV / 2$, we have the following expressions for the trapezoid control points in terms of the photosensor sites x_A and x_B at both ends of the accumulation interval:

$$x_0 = x_A - w \, , \tag{6.1a}$$

$$x_1 = \text{MIN}\ (x_A + w \, , x_B - w \,) \, , \tag{6.1b}$$

$$x_2 = \text{MAX}\ (x_A + w \, , x_B - w \,) \, , \tag{6.1c}$$

$$x_3 = x_B + w \, . \tag{6.1d}$$

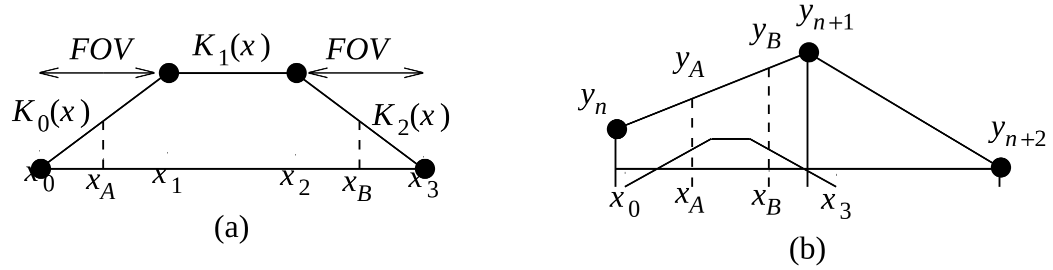

Figure 6: (a) Kernel K; (b) K applied to data.

Kernel K is defined as

$$K(x) = K_0(x) + K_1(x) + K_2(x) \, , \tag{6.2}$$

where

$$K_0(x) \;=\; \frac{x - x_0}{x_1 - x_0} \qquad \text{for } x_0 \le x < x_1\,, \tag{6.3a}$$

$$K_1(x) \;=\; 1 \qquad \text{for } x_1 \le x < x_2\,, \tag{6.3b}$$

$$K_2(x) \;=\; 1 - \frac{x - x_2}{x_3 - x_2} \qquad \text{for } x_2 \le x < x_3\,. \tag{6.3c}$$

Figure 6b depicts K being applied to the underlying irradiance function H. Each observed area sample is now a weighted integral:

$$F_n \;=\; W_n \int_{x_0}^{x_3} H(x)\, K(x)\, dx\ . \tag{6.4}$$

Since $K(x)$ has three components, we may compute F_n in parts:

$$F_n \;=\; \sum_{i=0}^{2} F_{n_i} \;=\; W_n \sum_{i=0}^{2} \int_{x_i}^{x_{i+1}} H(x)\, K_i(x)\, dx\ . \tag{6.5}$$

Integrating over the three intervals separately permits us to use the results of Section 5 in computing the unknown linear spline control points. Rather than considering points A and B, we consider whether x_i and x_{i+1} lie in one or two spline segments, for $0 \le i \le 2$.

6.1. Area Samples — Case 1: Trapezoid Interval Lies in One Spline Segment

Consider the case where a trapezoid interval lies entirely in one spline segment. The area sample contribution F_{n_i} for interval i is the weighted integral under the line $H(x) = m_H x + b_H$ from x_i to x_{i+1}, with the weights taken from $K_i(x) = m_{K_i} x + b_{K_i}$. This yields

$$\begin{aligned} F_{n_i} \;&=\; W_n \int_{x_i}^{x_{i+1}} H(x)\, K_i(x)\, dx \\ &=\; W_n \int_{x_i}^{x_{i+1}} \left[\, m_H\, m_{K_i}\, x^2 + (m_H\, b_{K_i} + m_{K_i}\, b_H)\, x + b_H\, b_{K_i} \right] dx \\ &=\; W_n \left[\, \frac{m_H\, m_{K_i}}{3}\, \Delta x_i^{\,3} + \frac{m_H\, b_{K_i} + m_{K_i}\, b_H}{2}\, \Delta x_i^{\,2} + b_H\, b_{K_i}\, \Delta x_i \right]\ , \end{aligned} \tag{6.6}$$

where $\Delta x_i = x_{i+1} - x_i$. We further simplify F_{n_i} for each of the three intervals by substituting the following values into Eq. (6.6):

Interval	m_{Ki}	b_{Ki}	m_H	b_H
0	$1/\Delta x_0$	0	$\Delta y_0/\Delta x_0$	y_0
1	0	1	$\Delta y_1/\Delta x_1$	y_1
2	$-1/\Delta x_2$	1	$\Delta y_2/\Delta x_2$	y_2

Note that $\Delta y_i = y_{i+1} - y_i = H(x_{i+1}) - H(x_i)$. This substitution yields the following results for all three intervals:

$$F_{n_0} = W_n \left[\frac{2\,\Delta y_0 + 3y_0}{6} \Delta x_0 \right] = W_n \left[\frac{(y_0 + 2y_1)(x_1 - x_0)}{6} \right] , \tag{6.7a}$$

$$F_{n_1} = W_n \left[\frac{\Delta y_1 + 2y_1}{2} \Delta x_1 \right] = W_n \left[\frac{(y_1 + y_2)(x_2 - x_1)}{2} \right] , \tag{6.7b}$$

$$F_{n_2} = W_n \left[\frac{\Delta y_2 + 3y_2}{6} \Delta x_2 \right] = W_n \left[\frac{(2y_2 + y_3)(x_3 - x_2)}{6} \right] . \tag{6.7c}$$

As in the simpler rectangular case, note that we are not actually given the y_i's; they are determined by interpolating between the unknown control points using the known LSA x_i positions. Without loss of generality, we normalize the parameters so that $x_n = 0$, $x_{n+1} = 1$, and $0 \le x_i, x_{i+1} \le 1$ for $0 \le i \le 2$, to yield

$$y_i = y_n\,(1 - x_i) + y_{n+1}\,(x_i) , \tag{6.8a}$$

$$y_{i+1} = y_n\,(1 - x_{i+1}) + y_{n+1}\,(x_{i+1}) . \tag{6.8b}$$

Substituting these expressions into Eq. (6.7) yields the following relationships between F_{n_i} and the unknown control points:

$$\frac{6F_{n_0}}{W_n} = \left[y_n\ (3-x_0-2x_1) + y_{n+1}\ (x_0+2x_1) \right]\ (x_1-x_0)$$

$$= y_n \left[x_0^2 - 2x_1^2 + x_0x_1 - 3x_0 + 3x_1 \right] + y_{n+1} \left[-x_0^2 + 2x_1^2 - x_0x_1 \right] , \tag{6.9a}$$

$$\frac{2F_{n_1}}{W_n} = \left[y_n\ (2-x_1-x_2) + y_{n+1}\ (x_1+x_2) \right]\ (x_2-x_1)$$

$$= y_n \left[x_1^2 - x_2^2 - 2x_1 + 2x_2 \right] + y_{n+1} \left[-x_1^2 + x_2^2 \right] , \tag{6.9b}$$

$$\frac{6F_{n_2}}{W_n} = \left[y_n\ (3-2x_2-x_3) + y_{n+1}\ (2x_2+x_3) \right]\ (x_3-x_2)$$

$$= y_n \left[2x_2^2 - x_3^2 - x_2x_3 - 3x_2 + 3x_3 \right] + y_{n+1} \left[-2x_2^2 + x_3^2 + x_2x_3 \right] . \tag{6.9c}$$

Note that Eq. (6.9b) is identical to the expression in Eq. (5.5) because we had derived that result with a unit area kernel. We may therefore simplify Eq. (6.9b) to match Eq. (5.6). In addition, Eqs. (6.9a) and (6.9c) can be reduced to the form $6F_{n_i}/W_n = y_n\,[3\,(x_{i+1}-x_i) - k_i] + y_{n+1}k$ for $i = 0$ and $i = 2$.

6.2. Area Samples — Case 2: Trapezoid Interval Straddles Two Spline Segments

Consider the case where a trapezoid interval straddles two spline segments, between $[x_n, x_{n+1}]$ and $[x_{n+1}, x_{n+2}]$. F_{n_i} is now expressed as the sum of two area contributions, spanning $[x_i, x_{n+1}]$ and $[x_{n+1}, x_{i+1}]$, respectively. Without loss of generality, we normalize the parameters so that $x_n = 0$, $x_{n+1} = 1$, $x_{n+2} = 2$, and $0 \le x_i, x_{i+1} \le 1$, thus yielding

$$y_i = y_n\ (1-x_i) + y_{n+1}\,(x_i)\ , \tag{6.10a}$$

$$y_{i+1} = y_{n+1}\,(1-x_{i+1}) + y_{n+2}\,(x_{i+1})\ , \tag{6.10b}$$

for $0 \le i \le 2$. In terms of Eq. (6.7), the sample values may be written

$$F_{n_0} = W_n \left[\frac{(y_0 + 2y_{n+1})\,(1 - x_0)}{6} \right] + W_n \left[\frac{(y_{n+1} + 2y_1)\,x_1}{6} \right] , \qquad (6.11a)$$

$$F_{n_1} = W_n \left[\frac{(y_1 + y_{n+1})\,(1 - x_1)}{2} \right] + W_n \left[\frac{(y_{n+1} + y_2)\,x_2}{2} \right] , \qquad (6.11b)$$

$$F_{n_2} = W_n \left[\frac{(2y_2 + y_{n+1})\,(1 - x_2)}{6} \right] + W_n \left[\frac{(2y_{n+1} + y_3)\,x_3}{6} \right] . \qquad (6.11c)$$

Substituting the expressions for y_i and y_{i+1} into Eq. (6.11), we are left with the following expressions in terms of the unknown control points:

$$\frac{6F_{n_0}}{W_n} = \left[y_n\,(1-x_0) + y_{n+1}x_0 + 2y_{n+1} \right] (1-x_0) + \left[y_{n+1} + 2y_{n+1}(1-x_1) + 2y_{n+2}x_1 \right] x_1$$

$$= y_n \left[(1-x_0)^2 \right] + y_{n+1} \left[(x_0+2)(1-x_0) + x_1(3-2x_1) \right] + y_{n+2} \left[2x_1^2 \right] , \qquad (6.12a)$$

$$\frac{2F_{n_1}}{W_n} = \left[y_n\,(1-x_1) + y_{n+1}x_1 + y_{n+1} \right] (1-x_1) + \left[y_{n+1} + y_{n+1}(1-x_2) + y_{n+2}x_2 \right] x_2$$

$$= y_n \left[(1-x_1)^2 \right] + y_{n+1} \left[1 - x_1^2 + (2-x_2)x_2 \right] + y_{n+2} \left[x_2^2 \right] , \qquad (6.12b)$$

$$\frac{6F_{n_2}}{W_n} = \left[2y_n\,(1-x_2) + 2y_{n+1}x_2 + y_{n+1} \right] (1-x_2) + \left[2y_{n+1} + y_{n+1}(1-x_3) + y_{n+2}x_3 \right] x_3$$

$$= y_n \left[2(1-x_2)^2 \right] + y_{n+1} \left[(2x_2+1)(1-x_2) + x_3(3-x_3) \right] + y_{n+2} \left[x_3^2 \right] . \qquad (6.12c)$$

Note that Eq. (6.12b) is identical to the expression in Eq. (5.10). This corresponds to the single unit area kernel interval considered in that section.

6.3. Solving for the Control Points

Given either of the two cases for the positions of x_i and x_{i+1}, we have Eqs. (6.9) and (6.12) to relate each area sample with the neighboring control points. Each area sample is actually composed of three contributions: one from each of the three intervals of the trapezoid kernel K. Each trapezoid interval, depending on whether it lies in one or two spline segments, adds a constraint to two or three linear spline control points, respectively. Since the three intervals each constrain an overlapping set of three control points, there may be up to five neighboring points that contribute to each area sample. Collectively, they yield a pentadiagonal system of equations shown below in Eq. (6.13):

$$
\begin{bmatrix}
b_0 & c_0 & d_0 & e_0 & & & \\
a_1 & b_1 & c_1 & d_1 & e_1 & & \\
 & . & . & . & . & . & \\
 & & a_{n-4} & b_{n-4} & c_{n-4} & d_{n-4} & e_{n-4} \\
 & & & a_{n-3} & b_{n-3} & c_{n-3} & d_{n-3} \\
 & & & & a_{n-2} & b_{n-2} & c_{n-2} \\
 & & & & & a_{n-1} & b_{n-1}
\end{bmatrix}
\begin{bmatrix}
y_0 \\ y_1 \\ . \\ y_{n-4} \\ y_{n-3} \\ y_{n-2} \\ y_{n-1}
\end{bmatrix}
=
\begin{bmatrix}
F_0 \\ F_1 \\ . \\ F_{n-4} \\ F_{n-3} \\ F_{n-2} \\ F_{n-1}
\end{bmatrix}
$$

The matrix consists of one subdiagonal element and three superdiagonal elements. The elements a_i, b_i, c_i, d_i, and e_i are the weights of y_{i-1}, y_i, y_{i+1}, y_{i+2}, and y_{i+3}, respectively, as given in Eqs. (6.9) and (6.12). They are expressed in terms of the known x_i and x_{i+1} positions.

When the field of view FOV is nonzero, pixels beyond the image border must be considered when the photosensor is centered along the boundary. Because we limit FOV to be less than or equal to one dot size, we must not be concerned with addressing pixels beyond y_{-1} or y_n. In both of these cases, though, we apply the pixel replication boundary condition to get $y_{-1} = y_0$ and $y_n = y_{n-1}$. This boundary condition is reflected in diagonal elements b_0, d_{n-2}, and c_{n-1}. The missing a_0, e_{n-2}, and d_{n-1} terms that would apply to pixels beyond the image border must simply be added back into b_0, d_{n-2}, and c_{n-1}, respectively. Finally, the control points are evaluated by solving the band diagonal system of equations using an efficient LU decomposition algorithm optimized for band diagonal matrices [18].

7. Modeling the Image Irradiance Distribution

The previous two sections have described the image restoration algorithm assuming rectangular and trapezoidal kernels to account for the dynamic integration aperture. These kernels account for the combined effect of the point spread function and motion blur of each element in the LSA. One assumption maintained throughout the discussion has been that the image irradiance distribution H can be satisfactorily modeled by a piecewise linear model (see Fig. 4). The control points solved for in the pentadiagonal system are those of a linear spline. Had we desired a smoother underlying function for H then additional constraints would be needed in the system of equations and we could expect to have wider bands.

A higher-order fit to H, however, is actually undesirable in the present application. Intuitively, a smoother model prevents fast edge transitions to be modeled without excessive overshoots/undershoots near the discontinuities. This is akin to the Gibbs phenomenon that predicts ringing near edges when reconstructing a signal with a truncated set of frequency terms in the Fourier series. More specifically, this oscillatory response can be ascertained from Eq. (5.2), which yields an expression for y_{n+1} in terms of F_n and the previously computed control point y_n: $y_{n+1} = 2F_n - y_n$ when $X_{acc} = 1$. If we consider a step edge for the F_n values, we get oscillations after we cross the edge (see Fig. 7).

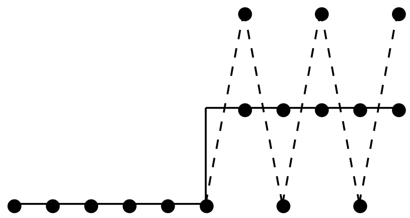

Figure 7: A piecewise linear fit to a step edge.

Notice that the area under each segment of the highly oscillatory linear reconstruction of H (depicted with dashed lines) remains satisfied. A problem, however, occurs when we introduce vibrations into the system and the intervals shift over which we compute the integral. In such cases, we can expect the reconstructed scanned imagery to have excessive ringing due to the underlying model rather than due to the shifting integration intervals. Smoother models for H do not improve matters. Therefore, we consider the effects of a piecewise constant approximation. The advantage of this approach is that discontinuities are readily handled. Because text and halftone imagery consists primarily of (near) step edges, this is an important consideration. Furthermore, the piecewise constant intervals are limited to a single dot size.

A piecewise constant fit to H is especially well-suited for step edges, as depicted by solid lines in Fig. 7. We may derive expressions for the constraints placed on the unknown control points by the area samples by making some simplifying substitutions in Eqs. (6.9) and (6.12). Note that the expression for each area sample contribution in Eq. (6.6) has coefficients in terms of m_H, the slope of the underlying piecewise linear model. Setting $m_H = 0$ provides the result we desire for the piecewise constant model. In particular, we let $\Delta y_i = 0$ in Eq. (6.7) for $i = 0$ and $i = 2$ and get the following results for the case when a trapezoid interval lies in one spline segment:

$$\frac{2F_{n_0}}{W_n} = y_n \left(x_1 - x_0 \right) , \tag{7.1a}$$

$$\frac{F_{n_1}}{W_n} = y_n \left(x_2 - x_1 \right) , \tag{7.1b}$$

$$\frac{2F_{n_2}}{W_n} = y_n \left(x_3 - x_2 \right) . \tag{7.1c}$$

The following results are obtained when a trapezoid interval straddles two spline segments:

$$\frac{2F_{n_0}}{W_n} = y_n \left(1 - x_0 \right) + y_{n+1} \left(x_1 \right) , \tag{7.2a}$$

$$\frac{F_{n_1}}{W_n} = y_n \left(1 - x_1 \right) + y_{n+1} \left(x_2 \right) , \tag{7.2b}$$

$$\frac{2F_{n_2}}{W_n} = y_n \left(1 - x_2 \right) + y_{n+1} \left(x_3 \right) . \tag{7.2c}$$

The piecewise constant model has the effect of diminishing the band width of the band diagonal system to no more than four nonzero elements per row.

8. Simulation of Scanning and Restoration

This section describes the steps taken in simulating the scanning of an image in the presence of vibrations and implementing the restoration algorithm. The simulation and restoration are performed in software. The integration time T_{acc}, photosensor field of view FOV, and sinusoid amplitudes A_i, frequencies f_i, and phase shifts ϕ_i (used to model the velocity error) are user-specified parameters passed to the program at run-time. Without loss of generality, we normalize the nominal velocity: $V_0 = 1$. This conveniently allows us to equate the integration distance X_{acc} to the accumulation time T_{acc} since $X_{acc} = V_0 T_{acc}$. Furthermore, all amplitudes can now be given directly as a percentage of nominal velocity. Once these parameters are given, the system proceeds as follows:

1) An image is read into the system to serve as a source of input for the scanner simulation. Each pixel of the input image is interpreted as an area sample of an image scanned under ideal conditions. That is, we assume $x_A = 0$, $x_B = X_{acc}$, and $FOV = 0$. Note that X_{acc} typically varies between 0.9 and 1.0, with $X_{acc} = 1.0$ being ideal.

2) These area samples are then used as the control points of the piecewise constant approximation to image irradiance function H. Were we interested in the control points of a linear spline approximation to H, we would begin with our boundary condition that $y_0 = F_0$. Substituting these values into Eq. (5.2) yields an expression for y_{n+1} in terms of F_n and the previously computed control point y_n:

$$y_{n+1} = 2F_n - y_n , \tag{8.1}$$

when $X_{acc} = 1$. In the more general case, we have

$$\begin{aligned} 2F_n &= \left(y_n + [y_n + (y_{n+1} - y_n) X_{acc}] \right) X_{acc} \\ &= y_n \, (2X_{acc} - X_{acc}^2) + y_{n+1} X_{acc}^2 . \end{aligned} \tag{8.2}$$

Therefore,

$$y_{n+1} = \frac{2F_n - y_n \, (2X_{acc} - X_{acc}^2)}{X_{acc}^2} . \tag{8.3}$$

Note that Eq. (8.3) yields the same result as Eq. (8.1) when $X_{acc} = 1.0$. Also, note that W_n has been set to 1 to ignore velocity nonuniformities while computing the control points.

3) The scanner simulation is applied to the spline to generate area samples degraded by an LSA moving at nonuniform velocity. A set of sinusoids with user-specified amplitudes, frequencies, and phases, is used to model the vibration. This requires us to compute LSA positions at uniform time intervals using Eq. (2.12). Due to the photosensor field of view, though, the accumulation span is actually wider. Furthermore, trapezoidal kernel K imposes three distinct weighting functions over each accumulation span. The spline must be weighted and integrated along these spans to produce area samples taken in the presence of vibration. We implement the evaluation of each area sample in three stages: one for each interval of the trapezoid. Eq. (6.1) is evaluated to determine the four points that delimit the intervals in each accumulation span. For each of the three intervals, we check whether its endpoints lie in the same spline segment or straddle two segments. The outcome of this test determines whether we accumulate the area contribution given in Eq. (7.1) or Eq. (7.2) to compute each area sample under the piecewise constant spline. In the case of the linear spline, area contributions given in Eq. (6.7) or Eq. (6.11) are used to compute each area sample.

4) These area samples **F** and the positions computed in Eq. (6.1) are then substituted into the band diagonal system of equations **K** in Eq. (6.13). As in step (3), the computation of the matrix elements for each row in Eq. (6.13) is computed in three phases. For each of the three intervals delimited by the points given in Eq. (6.1), we check whether its endpoints lie in the same spline segment or straddle two segments. The outcome of this test determines whether we accumulate the expressions given in Eq. (7.1) or Eq. (7.2) into the matrix elements for that row. For piecewise linear splines, the terms in Eq. (6.9) or Eq. (6.12) are accumulated into the matrix elements. Note that the factors of 2 and 6 in these equations are accounted for in the coefficients of the linear spline control points. In this manner, the sum after the three phases permits us to store $(F_{n0} + F_{n1} + F_{n2}) / W_n$, or simply F_n / W_n directly in the column vector F. Note that **F** changes for each image row; **K** remains the same and must therefore be evaluated only once.

5) We solve for the control points **Y** in $\mathbf{KY} = \mathbf{F}$. Ideally, **Y** should be identical to the control points computed in stage (2). An LU decomposition algorithm optimized for band diagonal matrices is used to solve for the control points **Y** [18].

6) The scanner simulation (integration) under ideal conditions is then applied to **Y** to produce the restored output. Ideal conditions simply refer to the integration of uniform spline intervals that are delimited by the control points. Although we can reduce the photosensor field of view to 0 (for ideal sensitivity function S and a $rect$ kernel K), we refrain from doing so to more clearly illustrate the restoration of images degraded solely by nonuniform LSA velocity.

An evaluation of the performance of the restoration is made by visually comparing the restored image with the original image that was read into the system in stage (1). Except for numerical round-off and clipping that may need to be performed at both ends of the intensity range, the resulting restorations are indistinguishable from the original input.

9. Examples

In the following examples we simulate an input scanner operating at 300 spi. A large vibration error (20%) is used in an attempt to render the image artifacts viewable after passing through the journal printing process. The parameters for the examples are listed below.

Scanner resolution	300 spi
Nominal velocity	2.5 inches/sec = 63.5 μm/msec
Vibration amplitude	20%
Vibration temporal frequency	7.0 Hz
Vibration spatial frequency	1 cy/mm
Vibration phase	0
Sensor dimensions	5 μm × 5 μm
Magnification	0.0826
Fractional T_{acc}	100%
FOV	50%

9.1. Periodic Lines

Note that the vibration frequency was chosen to be near the eye’s peak sensitivity at normal reading distance. A 300 spi scanner is simulated here because the images will print more accurately in this article than at 400 spi, as described in Section 4. For printing purposes, each grayscale 300 spi pixels was halftoned with an 8×8 0° cell. Halftoning in this manner will prevent interference between periodic image structure and the print screen. In each of the examples the piecewise constant image irradiance model has been employed. The scan direction is from left to right.

Figures 8a-c show a 4-on-4-off ideal periodic line image, the image scanned with vibratory motion, and the restored scanned image, respectively. Note that in the scanned image, the vibration frequency itself is not observable; it is a low-order beat, or interference, between the periodic image and the vibration that is observable, as described in Section 2. The restored image appears to be completely free of image defects.

9.2. Rotated Halftone Screens

Halftones are commonly scanned periodic images where the main periodic component could appear at a variety of angles. The amplitude of a given periodic halftone function is dependent upon the local gray level that the halftone represents. Figure 9a, from left to right, shows gray wedges halftoned at four screen angles that are commonly used for black (45°), cyan (15°), magenta (30°) and yellow (90°) color separtations, respectively. At the far right, the gray wedge is given as it would be rendered by an error diffusion algorithm. The halftone images scanned with vibratory motion are shown in Fig. 9b. We see that image areas that tend to have a strong periodic component in the scan direction most strongly show image defects. For example, the halftone screen commonly used for yellow is at 90°, and thus has a very strong periodic component in the scan direction and most strongly shows the beating defect. The halftone screen used for black is at 45°, and thus has a very weak (nearly constant) periodic component in the scan direction for most gray levels and barely shows the beating defect (see Section 2 on the effect of vibratory motion on constant images). In the halftone images and the error diffusion image, the gray levels that are represented by a stronger periodic function in the scan direction show more of the beating artifact than gray levels represented by weak period functions. A future study will analytically examine the relationship of the halftone design to vibration sensitivity.

The restored images are shown in Fig. 9c. Regardless of the magnitude of the degradation among the various halftones, the restoration has yielded images that are virtually free of all defects.

9.3. Text

Ideal, vibration-perturbated, and restored text images are shown in Fig. 10a-c, respectively. We see that the image defect appears as a stroke width or stroke darkness variation. Again, the restoration method presented above has generated an ouput image that is essentially free of image defects.

10. Summary

Images scanned in the presence of mechanical vibrations are subject to artifacts such as brightness fluctuation and geometric warping. This work has demonstrated how to invert these distortions and produce output consistent with a scanner operating under ideal conditions. The digital image restoration algorithm described in this paper makes use of the instantaneous velocity of the linear sensor array to reconstruct an underlying piecewise linear model of the irradiance distribution. That reconstructed image is then suitable for resampling under ideal scanning conditions to produce the restored output. The algorithm was demonstrated on simulated scanned imagery with operating parameters taken from a typical document scanner.

11. References

[1] S. C. Som, ‘‘Analysis of the effect of linear smear on photographic images,’’ *J. Opt. Soc. Am.* 61, 859-864 (July 1971).

[2] D. Wulich and N. S. Kopeika, ‘‘Image resolution limits resulting from mechanical vibrations,’’ *Opt. Eng.* 26(6), 529-533 (June 1987).

[3] O. Hader, I. Dror, and N. S. Kopeika, ‘‘Image resolution limits resulting from mechanical vibrations. Part IV: real-time numerical calculation of optical transfer functions and experimental verification,’’ *Opt. Eng.* 33(2), 566-577 (Feb 1994).

[4] R. Loce and W. Lama, ‘‘Exposure Strobing in Photocopiers,’’ *Journal of Imaging Science*, 32(6), 238-247 (Nov/Dec 1988).

[5] F. Bestenreiner, U. Geis, J. Helmberger, and K. Stadler, ‘‘Visibility and Correction of Periodic Interference Structures in Line-by-Line Recorded Images,’’ *J. Appl. Phot. Engr.* 2, 86-92 (1976).

[6] K. Takiguchi, T. Miyagi, A. Okamura, H. Ishoshi, and F. Shibata, ‘‘Effect of Photoreceptor Drum Rotational Speed Variation on Laser Beam Printer Halftone Reproduction,’’ *Proceedings of the SPSE Third International Congress*: *Recent Advances in Non−Impact Printing Technologies*, 168-172, San Francisco (8/86).

[7] D. Haas, ‘‘Contrast Modulation in Halftone Images Produced by Variation in Scan Line Spacing,’’ *J. Imaging Tech.* 15, 46 (1989).

[8] P. Schubert, ‘‘Periodic Image Artifacts from Continuous-Tone Laser Scanners,’’ *Appl. Opt.* 25(21) 3880-3884 (1986).

[9] R. Firth, D. Kessler, E. Muka, M. Noar, and J. Owens, ‘‘A Continuous Tone Laser Color Printer,’’ *J. Imaging Tech.* 14, 78 (1988).

[10] P. Burns, M. Rabbani, and L. Ray, ‘‘Analysis of Image Noise due to Position Errors in Laser Writers,’’ *Appl. Opt.* 25, 2158-2168 (1986).

[11] P. Melnychuck and R. Shaw, ‘‘Fourier Spectra of Digital Halftone Images Containing Dot Position Errors,’’ *J. Opt. Soc. Am.* 5(8), 1328-1338 (1988).

[12] S. Bloomberg and P. Engeldrum, ‘‘Color Error due to Pixel Placement Errors in a Dot Matrix Printer,’’ *Proceedings of the SPSE Third International Congress*: *Recent Advances in Non-Impact Printing Technologies*, 257-260 (Aug. 1986).

[13] R. Loce and W. Lama, ‘‘Halftone Banding due to Vibrations in a Xerographic Image Bar Printer,’’ *Journal of Imaging Technology*, 16(1), 6-11 (1990).

[14] R. Loce, W. Lama, and M. Maltz, ‘‘Modeling Vibration-Induced Halftone Banding in a Xerographic Laser Printer,’’ *Journal of Electronic Imaging*, 4(1), 48-61 (Jan. 1995).

[15] R. Loce and G. Wolberg, ‘‘Characterization of Vibration-Induced Image Defects in Input Scanners,’’ *SPIE Conf. on Document Processing II*, Proc. SPIE 2422, 350-357 (Feb. 1995).

[16] G. Wolberg and R. Loce, ‘‘Restoration of Images Degraded by Input Scanner Vibrations,’’ *SPIE Conf. on Document Processing II*, Proc. SPIE 2422, 358-369 (Feb. 1995).

[17] M. Abramowitz and I. A. Stegun, *Handbook of Mathematical Functions*, National Bureau of Standards, 1964.

[18] W. H. Press, S. A. Teukolsky, W. T. Vetterling, and B.P. Flannery, *Numerical Recipes in C*, Cambridge University Press, 1992.